Incidence Angle and Pitch-Chord Effects on Secondary Flows Downstream of a Turbine Cascade

A. Perdichizzi
Dipartimento di Meccanica,
Università di Brescia,
25060, Brescia, Italy

V. Dossena
Dipartimento di Energetica,
Politecnico di Milano,
20100, Milano, Italy

This paper describes the results of an experimental investigation of the three-dimensional flow downstream of a linear turbine cascade at off-design conditions. The tests have been carried out for five incidence angles from −60 to +35 deg, and for three pitch-chord ratios: s/c = 0.58, 0.73, 0.87. Data include blade pressure distributions, oil flow visualizations, and pressure probe measurements. The secondary flow field has been obtained by traversing a miniature five-hole probe in a plane located at 50 percent of an axial chord downstream of the trailing edge. The distributions of local energy loss coefficients, together with vorticity and secondary velocity plots, show in detail how much the secondary flow field is modified both by incidence and by cascade solidity variations. The level of secondary vorticity and the intensity of the crossflow at the endwall have been found to be strictly related to the blade loading occurring in the blade entrance region. Heavy changes occur in the spanwise distributions of the pitch-averaged loss and of the deviation angle, when incidence or pitch-chord ratio is varied.

Introduction

The operating conditions of a turbine profile may extend over quite a wide range. Changes of rotational speed and flow rate are the main cause for incidence angle and expansion ratio variations. Pitch-chord ratio may also vary, when the same profile is employed in various stages with different solidities.

In the aerodynamic development of a multistage turbine the knowledge of blade row performance in terms of loss and secondary flow angle distribution is of utmost importance, both for optimizing the design, and for predicting the overall efficiency at part loads. This is true especially in low aspect ratio stages where the secondary effects are often dominant. By using loss prediction methods based on empirical correlations such as those of Ainley and Mathieson (1951), Dunham and Came (1970) and Craig and Cox (1971), only limited information can be obtained; if a reliable estimation of the secondary flow effects at off-design conditions is desired, such methods are quite inadequate. Therefore the only way to get such precious information is to carry out an experimental investigation on the selected profiles.

In the last few years a very large number of experimental works on secondary flows in turbine cascades at design conditions have been carried out. These investigations aimed to clarify the details of three-dimensional flow development (e.g., Langston et al., 1977; Marchal and Sieverding, 1977; Sharma and Butler, 1987; Hodson and Dominy, 1987a; Yamamoto, 1987), to analyze the loss production mechanism (e.g., Moore and Adhye, 1985; Gregory-Smith et al., 1988a) and to determine the development of turbulence quantities (e.g., Moore et al., 1987; Zunino et al., 1987; Gregory-Smith et al., 1988b; Perdichizzi et al., 1989). On the other hand, very few papers are available in the published literature about secondary flows at off-design conditions. Yamamoto and Nouse (1988) have shown the influence of the incidence angle on the three-dimensional flow inside a linear cascade. The investigation refers to a low-velocity cascade at moderately positive and high negative incidences. Hodson and Dominy (1987b) have reported secondary flows downstream of a high-speed linear cascade under off-design conditions, including incidence angle, pitch-chord ratio, Reynolds number, and inlet boundary layer thickness variations.

The present work aims partially to overcome the lack of data at off-design conditions, by providing detailed information on the three-dimensional flow downstream of a turbine cascade, within a wide range of incidence angles and for different cascade solidities. An additional objective of the work is to supply a set of experimental data under heavy off-design conditions, to be used for the validation of a three-dimensional viscous flow computational method (Bassi and Savini, 1992).

Experimental Details

The experimental investigation was carried out in the CNPM (Centro Nazionale per Ricerche sulla Propulsione e sull'Energetica, Milano) transonic wind tunnel, which is a blow down facility for linear turbine cascade tests. The test section, 50 mm high and 400 mm wide, allows the support of cascades with a relatively large number of blades.

The cascades consisted of blades scaled from a high-pressure stage steam turbine nozzle with an aspect ratio $h/b = 1.47$ and a geometric turning angle $\Delta\beta' = 89.4$ deg. Tests have

Contributed by the International Gas Turbine Institute and presented at the 37th International Gas Turbine and Aeroengine Congress and Exposition, Cologne, Germany, June 1-4, 1992. Manuscript received by the International Gas Turbine Institute February 11, 1992. Paper No. 92-GT-184. Associate Technical Editor: L. S. Langston.

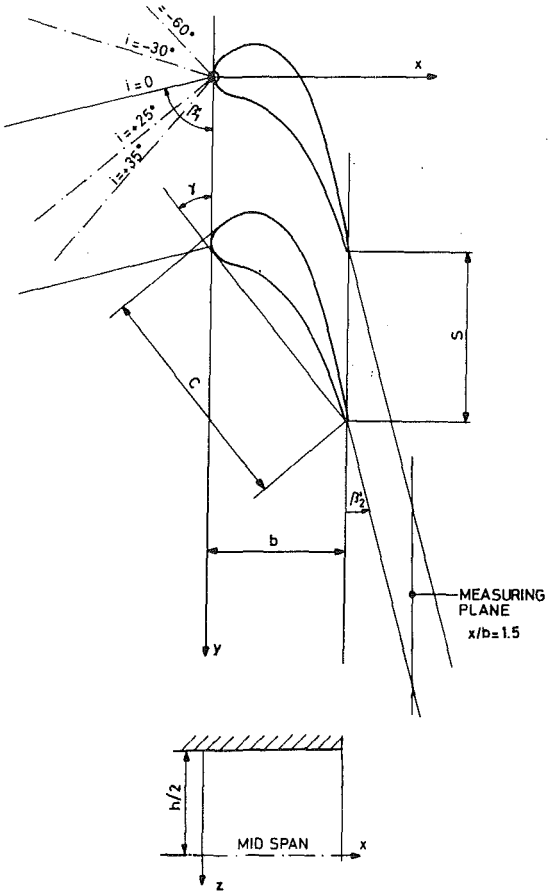

Fig. 1 Cascade geometry

been carried out on three different cascades characterized by different solidities corresponding to s/c = 0.58, 0.73, 0.87.

The changes in pitch-cord ratio were obtained simply by shifting the blades pitchwise; as a consequence, the number of blades of the cascade had to be consistently modified with the pitch value (Z = 11, 9, 8). The central blades have been instrumented by static pressure at the midspan section, in order to support information about profile velocity distribution. The cascade geometry and the relevant geometric data are shown in Fig. 1 and Table 1.

The measurements have been carried out by means of a fully automated computer-controlled data acquisition system. Downstream measurements have been carried out at a plane located at 50 percent of an axial chord from the trailing edge, by means of a miniaturized five-hole conical pressure probe presenting a head diameter of 1.5 mm. The measurement plane

Table 1 Cascade geometric data

Chord length, c	55.2 mm
Axial chord, b	34.0 mm
Aspect ratio, h/b	1.47
Inlet blade angle, β_1'	76.1 deg
Outlet blade angle, β_2'	14.5 deg
Blade turning angle, $\Delta\beta'$	89.4 deg
Stagger angle, γ	39.9 deg

Table 2 Inlet boundary layer at design conditions

Displacement thickness, δ^*	2.90 mm
Momentum thickness, θ	2.18 mm
Form factor, H	1.31
Inlet loss, $\zeta_1 \times 100$	1.18
Inlet Mach number, M_1	0.15
Outlet Mach number, M_{2is}	0.70
Reynolds number, $Re_2 \times 10^6$	0.84

was selected far enough from the trailing edge, where most of the energy dissipation has already taken place and the loss coefficient is representative of the overall energy dissipation. The measuring grid has been defined by 10 points in spanwise direction and by a 2 mm step in pitchwise direction. Further details about the experimental apparatus and the measuring procedure can be found from Bassi and Perdichizzi (1987) and Osnaghi and Perdichizzi (1990).

The cascades have been tested at five different incidence angles, i.e., −60, −30, 0, +25, +35 deg and for Mach numbers ranging from 0.3 up to 0.9. As the Mach number influence on secondary flows has already been treated in a previous paper (Perdichizzi, 1990), the following discussion refers mainly to the design expansion ratio, corresponding to M_{2is} = 0.7.

The results are presented in terms of kinetic energy loss coefficient, secondary velocity, and streamwise vorticity plots. The secondary velocity at a given pitchwise position is defined as the projection of the local velocity vector onto a plane normal to the midspan velocity. The local kinetic energy loss coefficient is defined as:

$$\zeta = \frac{q_{2is(y,z)}^2 - q_{2(y,z)}^2}{\overline{q}_{2isMS}^2}$$

The streamwise vorticity ω_s has been calculated from the axial and tangential components ω_x and ω_y; the first is directly estimated by the experimental results while ω_y is evaluated as indicated by Gregory-Smith et al. (1988a), using the spanwise component of the Crocco relation and by assuming total enthalpy to be constant. The presented vorticity contours have been nondimensionalized by using the inlet free stream velocity and the blade chord.

The upstream flow has been traversed by a flattened Pitot probe at x/b = 1.0 to determine the inlet boundary layer profile, whose integral parameters are presented in Table 2. The inlet loss is referred to the outlet isentropic condition. No significant changes of these parameters have been found for the considered incidence angles.

Nomenclature

b = axial chord
c = chord
h = span
H = form factor or horseshoe
i = incidence angle
M = Mach number
q = velocity
Re = Reynolds number = qc/ν
s = pitch
s, n, z = flow coordinate system
S = separation line
SKE = secondary kinetic energy = $\int v_2^2 + w_2^2/\overline{q}_{2isMS}^2\, dydz$
u, v, w = velocities along s, n, z
x, y, z = cascade coordinates
Z = number of blades
β = flow angle (from tangential)
β' = blade angle (from tangential)
γ = stagger angle (from tangential)
δ^* = boundary layer displacement thickness
θ = boundary layer momentum thickness
ζ = energy loss coefficient
ν = kinematic viscosity
ω = vorticity

Subscripts

1 = inlet
2 = traverse plane
2is = downstream isentropic
MS = midspan
p = pressure side
s = suction side or streamwise
SEC = secondary

Superscripts

$\overline{\ }$ = pitchwise averaged
$\overline{\overline{\ }}$ = pitch and spanwise averaged

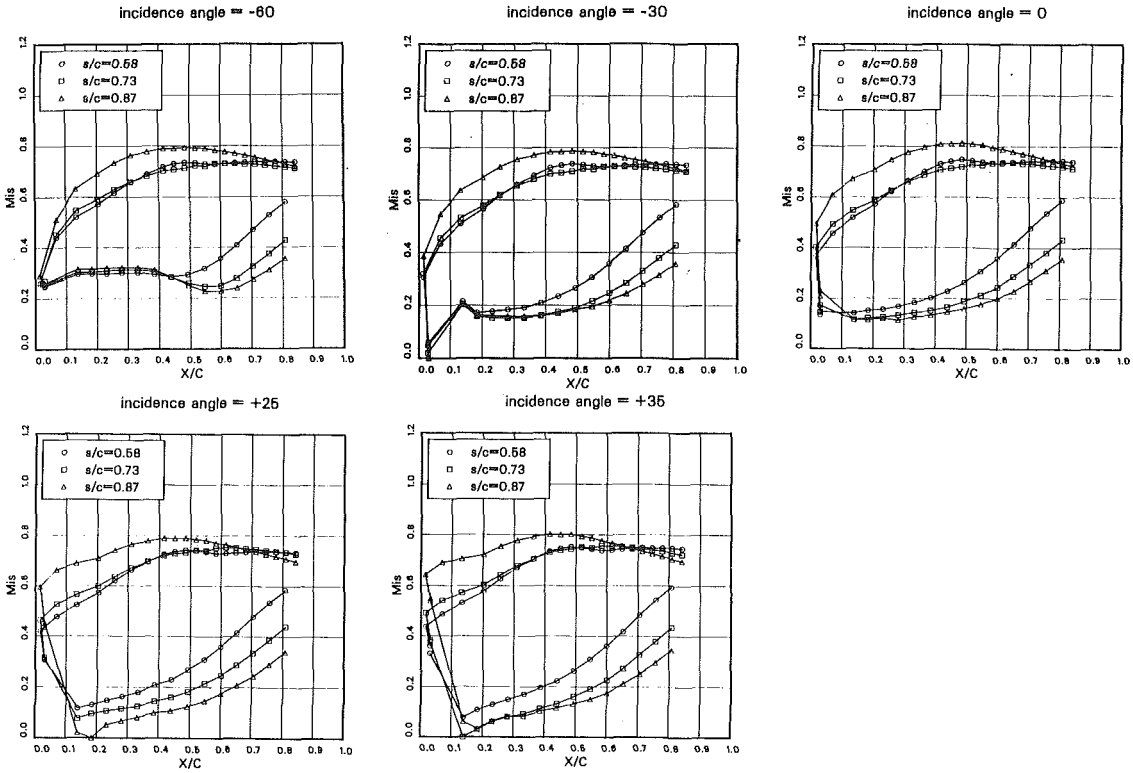

Fig. 2 Midspan insentropic Mach number distributions

Midspan Flow

The isentropic Mach number distributions measured at the midspan section for all the examined test conditions are presented in Fig. 2.

Referring to the design inlet flow angle, it can be seen that most of the flow acceleration takes place at the leading edge, producing the maximum blade loading just in the entrance region; beyond $x/c = 0.5$ the pressure on the suction surface remains constant, and the blade loading is reduced.

When the pitch is increased, the blade loading rises significantly everywhere along the blade. This is consistent with the larger momentum variation throughout the cascade. At the maximum s/c a greater acceleration, followed by a slight diffusion, takes place on the suction surface; on the pressure surface the velocity remains low for much of the blade, increasing only in the last part. The location of the stagnation point does not appear to be significantly influenced by the pitch-chord ratio.

Plots relating to incidence angles other than $i = 0$ show that the pressure distribution is strongly affected over much of the profile by the inlet flow angle variation.

At positive incidences the stagnation point moves downstream on the pressure side (up to about $x/c = 0.15$–0.20), producing an increase of circulation around the profile, and thus determining higher pressure differences between pressure and suction side in the entrance region. It has to be noticed that this effect becomes more important when increasing the pitch-chord ratio. It is not clear whether a separation bubble exists on the first part of the suction surface.

Decreasing the incidence below the nominal value, the blade loading at inlet undergoes a marked reduction and the stagnation point shifts upstream up to $x/c = 0.0$. At $i = -60$ the constant-pressure region occurring on the pressure surface for all the pitches suggests that a wide separation bubble exists. Then the boundary layer reattaches, presumably turbulent, at about $x/b = 0.4$. The diffusion behind the leading edge overspeeding is responsible for this separation. It is supposed that a less extended separation occurs at $i = -30$.

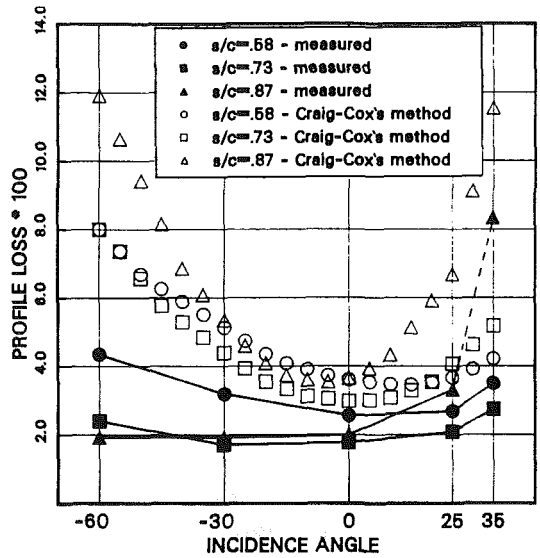

Fig. 3 Profile losses

It should be noticed that in the rear part of the profile the pressure distribution remains practically unchanged for all incidence angles.

The measured profile losses are presented in Fig. 3 together with the values predicted by the Craig-Cox method. The experimental data show a rather marked insensitivity of the profile loss to incidence, which is to be related to the thick and rounded leading edge of the profile.

The effects of the separation occurring at the minimum incidence become more important for the smallest pitch.

It should be pointed out that the steep increase of the loss found at $i = +35$ for the largest pitch is not a two-dimensional effect. As will be presently shown, the secondary flow effects in this condition are so conspicuous that they reach the midspan

section and no pure two-dimensional flow may be considered. The same consideration applies to the midspan outlet flow angle, which, under the above conditions, increases considerably (Fig. 4).

As far as the prediction is concerned, a relatively good agreement with the experiments at the design inlet angle can be noticed; the profile loss is slightly overestimated, and the pitch-chord influence is well enough captured. However, moving away from the design condition, the Craig-Cox method significantly overestimates the profile loss for both positive and negative incidences, providing unacceptable results.

Oil Flow Visualizations

To provide some information on the vortex structure developing inside the blade passage, surface oil flow visualizations have been carried out at three different inlet angles. As is well known, this technique allows one to follow the behavior of the various vortices, as it provides the traces of the near surface flow. Figure 5 shows a comprehensive view of suction surface and endwall visualizations obtained at $i = -30$, at the design inlet angle, and at $+25$ deg of incidence.

The primary separation lines, S_{1p}, S_{1s}, associated with the upstream boundary layer separation are easily visible at all the incidences, while the secondary ones S_{2p}, S_{2s}, corresponding to the horseshoe vortex separation from the endwall, can be clearly detected only at $i = +25$.

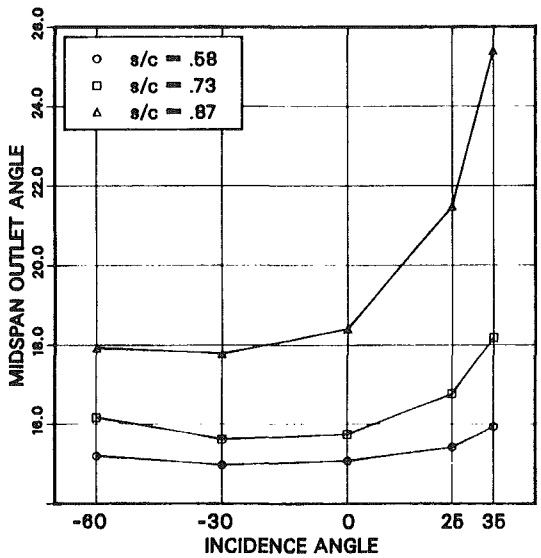

Fig. 4 Outlet flow angle

The flow field configuration appears to be greatly affected by the inlet angle. As the incidence angle is increased, the separation lines move significantly upstream of the leading edge.

At $i = -30$, the distance from the leading edge of the saddle point related to S_1 is about 0.10 c, while at $i = +25$ it becomes 0.23 c. Also the point where the separation line S_{1p} impacts the suction surface shifts significantly upstream: It moves from $x/b = 0.70$ ($i = -30$) to $x/b = 0.61$ ($i = 0$), up to $x/b = 0.45$ ($i = +25$). In a similar way the corresponding point related to S_{1s} moves from $x/b = 0.38$ to $x/b = 0.24$, up to $x/b = 0.18$. This trend is an outcome of the higher pressure difference driving the crossflow across the channel.

On the suction surface the separation line S_4 associated with the passage vortex is quite evident. The greater inclination of this line noticeable at $i = +25$ indicates a major intensity of the flow rotation within the vortex. Another clear effect is the increasing of the flow three-dimensionality: At the trailing edge the region affected by the passage vortex extends from $z/h = 0.12$ ($i = -30$) to $z/h = 0.19$ ($i = 0$), up to $z/h = 0.27$ ($i = +25$).

At $i = +25$ no traces of separation for the leading edge overspeeding are present on the suction surface. On the contrary, for $i = -30$ a separation bubble with a limited extent has been observed on the pressure side surface at $x/b = 0.10$.

Three-Dimensional Flow

Variation With Incidence. Figure 6 presents the results of the area traverses at the five incidences considered, for the design pitch-chord ratio (i.e., $s/c = 0.73$).

Zero Incidence. At the design inlet angle, the flow field appears consistent with the well-known secondary flow vortex structure. It should be pointed out that, as the measurement plane is relatively far from the trailing edge, turbulence and viscosity action have contributed to modify the flow configuration and to reduce partially the secondary vortex intensity with respect to the cascade exit plane. Relating to the classical model of the secondary flows in turbine cascades, i.e., Langston et al. (1977) and Sieverding (1985), the following features can be traced:

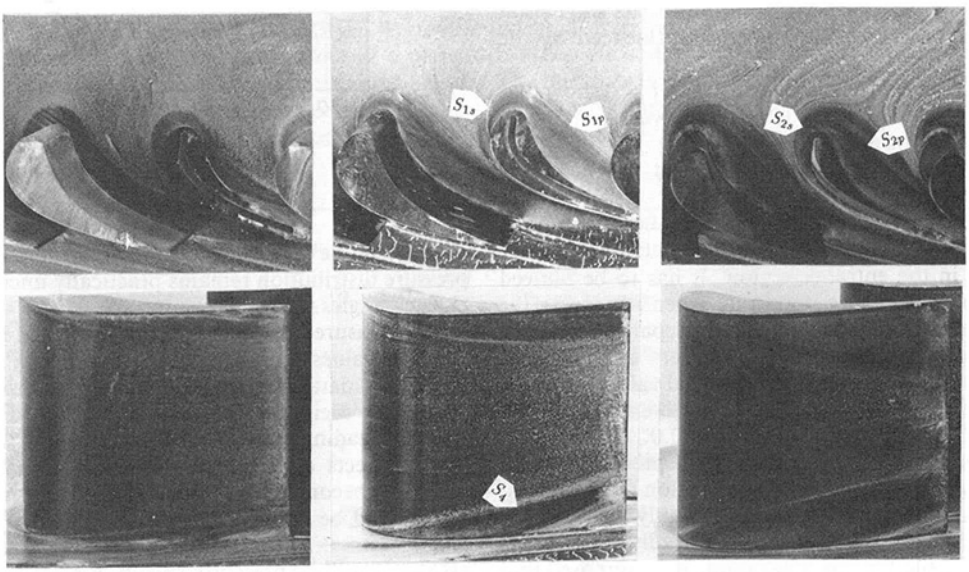

Fig. 5 Oil flow visualizations for $s/c = 0.73$ at $i = 30$, $i = 0$, and $i = +25$

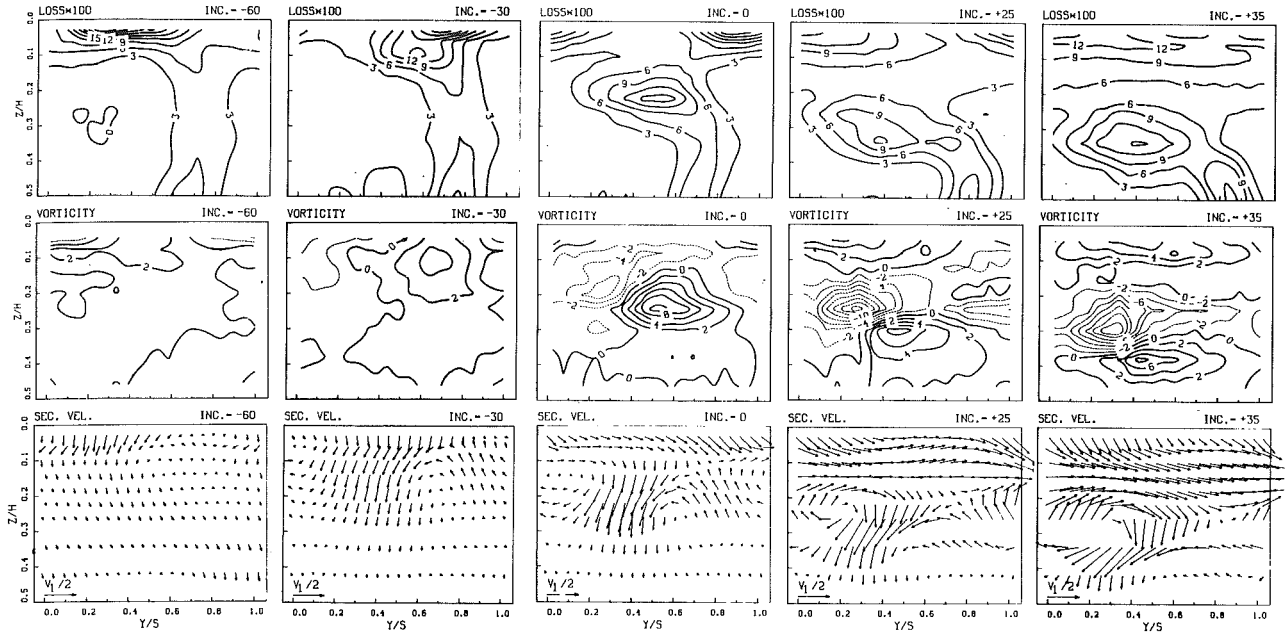

Fig. 6 Secondary velocity vectors, loss, and vorticity contours for *s/c* = 0.73

• The passage vortex, which can be identified by the clockwise rotating flow and by the negative vorticity core, appears to be relatively weak, as much of its secondary kinetic energy has been dissipated between the trailing edge and the measuring plane. However, an appreciable crossflow at the endwall remains, indicating the overall vorticity of the flow field.

• The trailing shed vorticity, which at the trailing edge originally developed as a vortex sheet, has been reorganized in a well-defined single vortex located across the wake. The shed vortex is still quite intense, as indicated by the secondary velocities and by the positive vorticity level. It is about twice the one found within the passage vortex.

• In the endwall region the spanwise secondary velocities, associated with positive vorticities, show the presence of the corner vortex. The loss core related to this vortex presents a high peak value (about 20 percent) and extends significantly in both pitchwise and spanwise direction. This loss, as suggested by Hodson and Dominy (1987a), is not only due to the dissipation of the secondary kinetic energy associated with the vortex, but it is also the result of the new endwall boundary layer swept toward the suction surface by the endwall crossflow.

• The wake appears significantly distorted toward the suction side, as the mixing process has been heavily influenced by the shed-passage vortex interaction. The position of loss core on the suction side of the wake coincides roughly with the vortex interaction region. The extension of this loss region and its distance from the endwall may be considered an index of the intensity of the secondary flow phenomena.

• No traces of the suction side leg of the horseshoe vortex are visible. Presumably it has been swept by the passage vortex.

Positive Incidence. As is well known, the secondary flow phenomena in a turbine cascade are considerably affected by the main flow deflection. This can be simply derived from the so-called transport vorticity equation, which is obtained by forming the curl of the full Navier–Stokes equation. In an intrinsic coordinate system the streamwise component can be written as follows:

$$\frac{D\omega_s}{Dt} = \omega_s \frac{\partial u}{\partial s} + \omega_n \frac{\partial u}{\partial n} + \omega_z \frac{\partial u}{\partial z} + \nu \nabla^2 \omega_s$$

If the viscous term is neglected, it follows that in the entrance region of a linear turbine cascade the rate of change of the streamwise vorticity ω_s depends only on the normal vorticity ω_n (due to the inlet boundary layer) and on the velocity gradients $\partial u/\partial n$ in the normal direction, as ω_s and ω_z are zero. Therefore when the incidence angle is increased, larger secondary flow effects must be expected, as larger velocity gradients take place between suction and pressure surface (see Fig. 2). The same feature may be drawn if s/c is increased.

Referring to the traverse results at $i = +25$ and $i = +35$, presented in Fig. 6, it can be seen that by increasing the incidence the secondary flow field experiences dramatic changes:

• The negative vorticity level increases considerably, denoting a much more intense passage vortex. This effect is a direct consequence of the high blade loading taking place in the entrance region (Fig. 2). At $i = +35$ the peak vorticity within the passage vortex is about 2.5 times the one found at design condition.

• The shed vorticity, on the contrary, remains roughly at the same level; this result is in contrast with the one presented by Hodson and Dominy (1987b), where a shed vorticity has been reported that rises appreciably at positive incidences. As the incidence is increased, a second positive vorticity core appears in the endwall region, showing a stronger intensity of the corner vortex.

• Both passage and shed vortex migrate toward the midspan, therefore the extension of the two-dimensional flow from the midspan section is progressively reduced.

• In most of the flow field the secondary velocities grow considerably, reaching the same order of magnitude of the inlet velocity. At the endwall there is an intense crossflow, which extends to about 20 percent of the blade height, revealing a large amount of the overall streamwise vorticity.

• The loss core on the suction side of the wake shifts toward the midspan in agreement with the higher intensity of the passage vortex. The peak value remains practically unchanged, but the overall loss is much greater, because of the higher secondary velocities occurring in both the vortex and the endwall regions. A larger loss appears out also in the wake presumably due to the leading edge overspeeding.

Negative Incidence. At the considered negative incidences the flow turning $\Delta\beta$ is considerably reduced as it decreases from 88.2 (design value) to 27.7 deg ($i = -60$). The following effects can be observed:

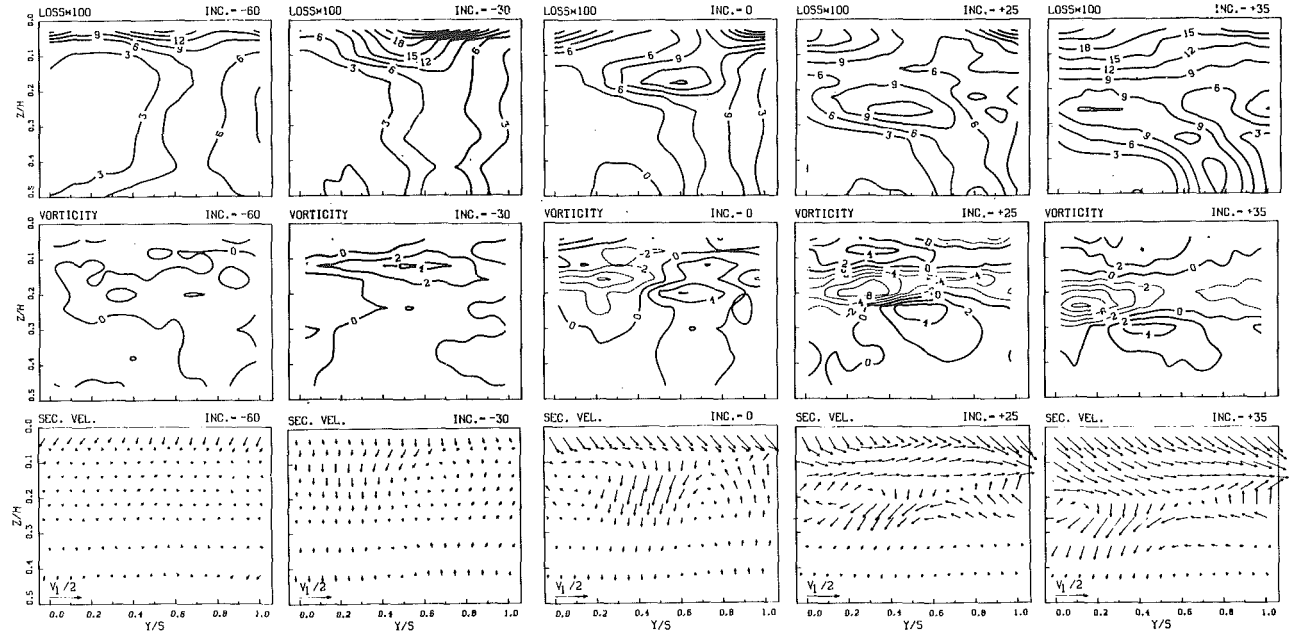

Fig. 7 Secondary velocity vectors, loss, and vorticity contours for $s/c = 0.58$

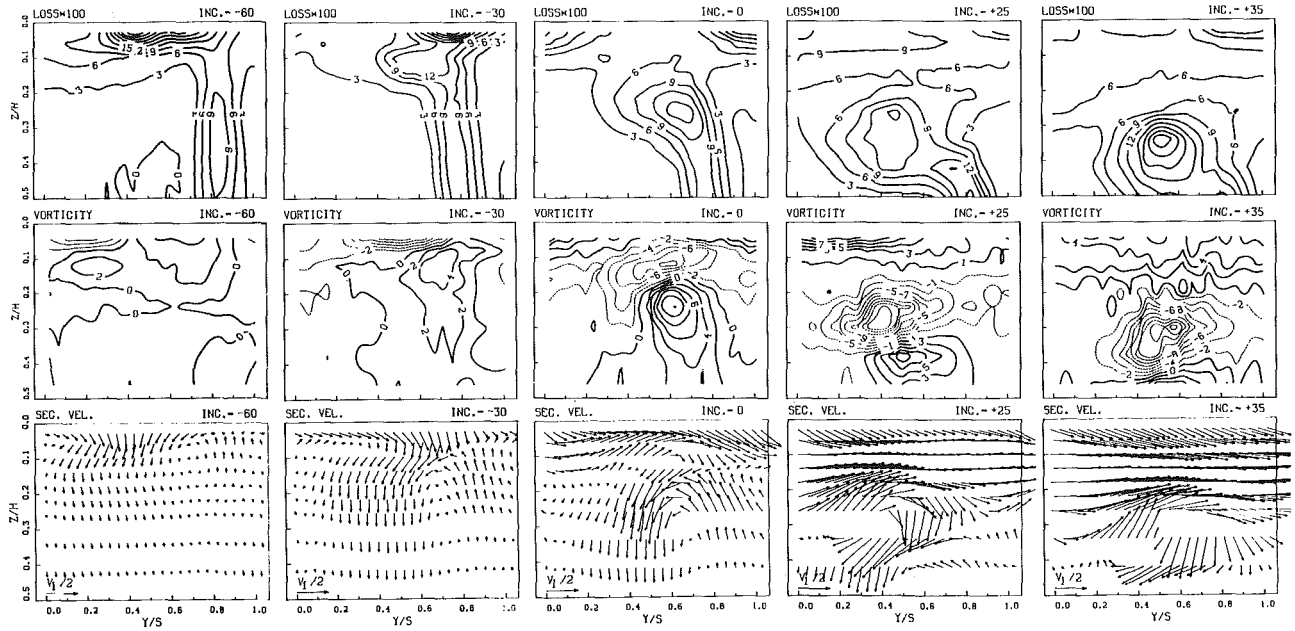

Fig. 8 Secondary velocity vectors, loss, and vorticity contours for $s/c = 0.87$

- The passage vortex experiences a drastic weakening and the secondary velocities in general become quite small. Both positive and negative vorticity are substantially lower and therefore the three-dimensional effects remain confined in the endwall region, leaving a two-dimensional flow along most of the blade height.
- On the pressure side of the wake, relatively far from the shed vortex, a clockwise rotating vortex is visible that should be mostly attributed to the pressure side leg of the horseshoe vortex, as suggested by Yamamoto and Nouse (1988). Indeed, at negative incidence this vortex is presumably stronger because of the high turning angle around the leading edge and the related overspeeding. No evident effect of the vortex interaction with the separation bubble on the pressure side was noted.
- The crossflow between the pressure and the suction side of the channel, which at zero and positive incidence was quite intense, is virtually absent. However, a very thin crossflow is thought to exist in the layer closest to the wall. It turns out that the crossflow intensity is very sensitive to the blade loading on the first part of the profile, but much less to the loading at the rear, after most of the flow turning has occurred and the secondary flows have developed.
- At -60 deg of incidence the loss distribution does not appear to be largely modified with respect to a normal boundary layer. This is the effect of the absence of the rolling action of the passage vortex on the inlet boundary layer. There is a single loss core close to the endwall with a high peak value, that is about 25 percent. This should be mostly related to the new endwall boundary layer developed throughout the cascade fed into the passage vortex. A contribution is supposed to come also by the pressure side leg of the horseshoe vortex.

Variation With Pitch-Chord Ratio. The influence of the pitch variation on the secondary flow field can be seen by comparing the results of the exit area traverses for $s/c = 0.58$ and $s/c = 0.87$, presented in Figs. 7 and 8, respectively.

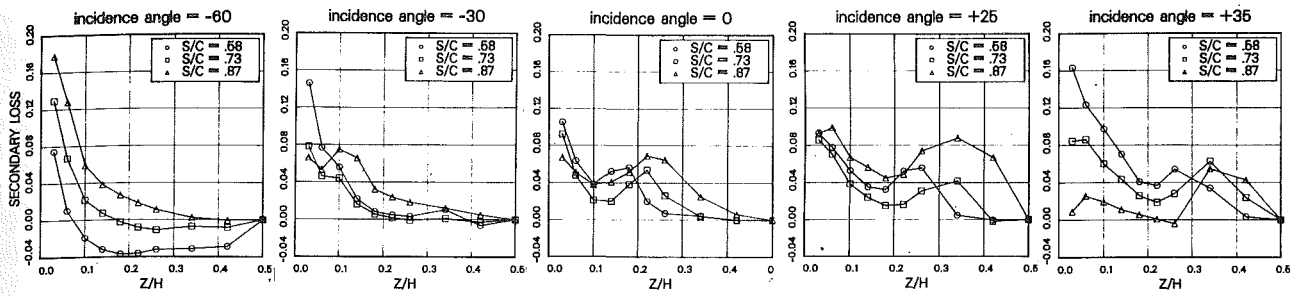

Fig. 9 Spanwise secondary loss distributions at different incidence angles

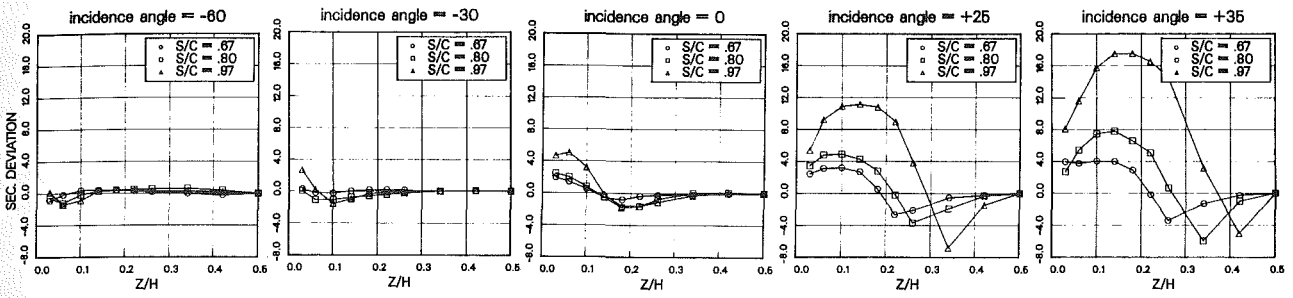

Fig. 10 Spanwise distributions of secondary flow angle deviation at different incidence angles

As the pitch is increased, the secondary velocities become generally greater for all the inlet conditions, but at positive incidence they undergo a truly dramatic growth; the flow field is dominated by a quite intense passage vortex and by an impressive crossflow extending up to $z/h = 0.26$. The peak of the negative vorticity is about twice the one at the smallest pitch and the secondary kinetic energy grows considerably all over the plane. These phenomena are the effects of the high loading occurring on the blade because of the contemporary presence of a large pitch-chord ratio and a high flow turning (Fig. 2).

There is another striking effect denoted by these results: Due to the occurrence of strong passage vortices, the region affected by the secondary phenomena extends up to the midspan; therefore the two passage vortices occurring in the upper and lower part of the blade passage interact. At this condition the overall loss is significantly increased; the loss contours present a wide core with a high peak value, at about 24 percent, located just in the center of the passage vortex. It should be noticed that at the midspan no wake can be discerned and therefore no two-dimensional flow can be considered. It is thought that in this very complex flow configuration the interaction of the two vortices, together with a presumed high turbulence and large Reynolds stresses, are responsible for such an important energy dissipation.

As far as the results for the smallest s/c, it has been found that the flow configuration is qualitatively similar to the one at the design cascade solidity, but with a general reduction of all the three-dimensional effects, i.e., the secondary velocities and the vorticity values. As noted above, when lower streamwise vorticities occur, the secondary phenomena are more confined in the endwall region and, even at a large incidence, there remains a two-dimensional flow for a wide blade height extent.

At the lowest incidence the wake appears to be heavily distorted to a major extent at the midspan. It is presumed that the H_p vortex interaction with the two-dimensional separation bubble on the pressure side beyond the leading edge (Fig. 2) is responsible for this phenomenon. In similar conditions, i.e., at large negative incidences, Yamamoto and Nouse (1988) have shown that new secondary flows arise that transport the low-momentum fluid within the separated region from the endwall toward the midspan. Here the low-energy fluid is accumulated and through a mixing process diffuses along the pitch; as a result midspan losses are greater than at the endwall. This result is surprising since, although the secondary vorticity was quite low, appreciable three-dimensional effects arose, affecting even the midspan flow.

It follows that also in these conditions it is not possible to consider the midspan flow as a two-dimensional reference flow, to be used for the estimation of the secondary effects.

An interesting feature that should be noted is that this phenomenon appears only at the smallest pitch-chord ratio; some weak traces can also be seen for the design pitch at the smallest incidence. It is presumed that the migration of the low-energy fluid toward the midspan occurs only when the passage vortex is very weak or virtually absent.

Mass-Averaged Results

The traverse data have been mass averaged across the pitch to get the spanwise distribution of the loss coefficient and of the exit angle. The secondary losses and deviation angles plotted in Figs. 9 and 10 are defined as:

$$\bar{\zeta}_{\mathrm{SEC}(z)} = \bar{\zeta}_{(z)} - \bar{\zeta}_{MS} \quad \Delta\beta_{\mathrm{SEC}(z)} = \bar{\beta}_{2MS} - \bar{\beta}_{2(z)}$$

The midspan values are assumed to be representative of the two-dimensional reference flow.

At the lowest incidence the loss distribution presents the maximum at the endwall and looks not too much different from the one of a boundary layer. For the lowest pitch the presence of negative values reveals that, as already noticed, the midspan flow is affected by secondary effects.

As the incidence angle is increased, the endwall loss decreases as the low-energy fluid is removed from the endwall by the passage vortex and is convected toward the midspan; as a consequence a peak is produced in the loss distribution. For larger pitch-chord ratios the position of the peak moves even more toward the midspan in agreement with the passage vortex behavior.

The yaw angle distribution at negative incidence presents very small underturning and overturning angles only close to the endwall, confirming the weakness of the secondary phenomena. Conversely, increasing the incidence, large overturning and underturning take place and the extension of the two-dimensional flow is progressively reduced. This trend is consistent with the greater intensity of passage and shed vortex previously shown.

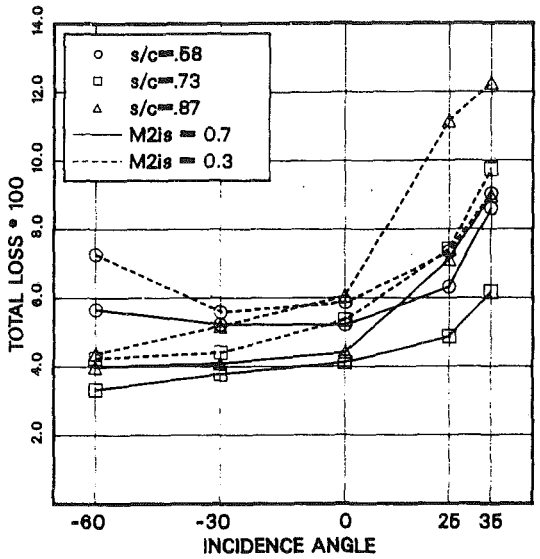

Fig. 11 Overall loss distributions for M_{2is} = 0.7 and for M_{2is} = 0.3

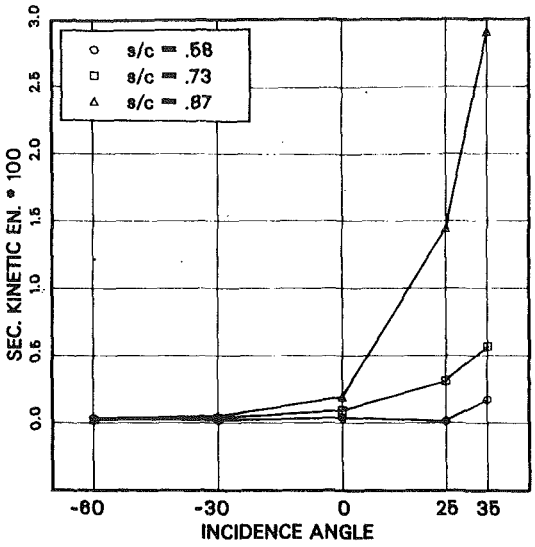

Fig. 13 Secondary kinetic energy

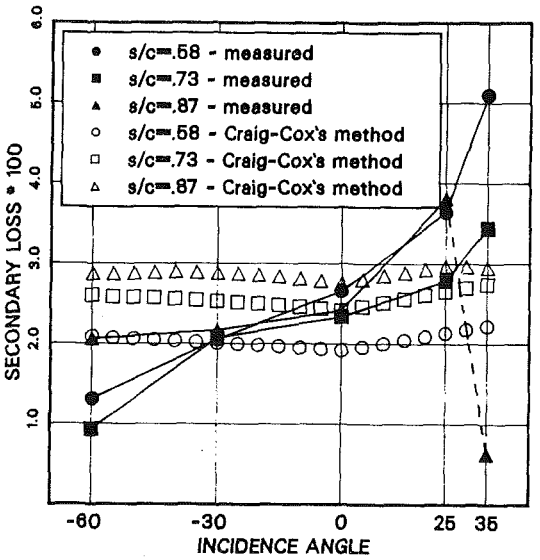

Fig. 12 Measured and predicted secondary losses

The large influence produced by the pitch-chord ratio should also be noted: At s/c = 0.87 both overturning and underturning angles are nearly twice the ones occurring at s/c = 0.73, and at i = +35 the difference between the maximum overturning and underturning becomes as great as 20 deg; however it has to be pointed out that in this last condition the secondary deviation distribution is not fully correct, as the three-dimensional effects have become so large as to affect the midspan values.

The overall loss $\bar{\bar{\zeta}}$, evaluated by the pitch and span mass average of the results, is plotted in Fig. 11, while Fig. 12 shows the secondary loss ζ_{SEC} obtained by subtracting the midspan value $\bar{\zeta}_{MS}$ from the overall loss. The dashed line indicates that the assumption considering the secondary flow superimposed on an undisturbed two-dimensional flow in the central part of the blade channel is no more valid. To complete the data, the overall secondary kinetic energy coefficient SKE is presented in Fig. 13.

It can be seen that the overall loss remains low even for high negative incidence, as the separation effects are counterbalanced by smaller secondary losses.

With increasing incidence, the overall loss undergoes a sharp increase that is particularly marked for the largest s/c. As shown in Fig. 13, this is mostly related to the growth of the secondary loss. However, at i = +35 for the largest pitch, it cannot be stated how much loss is due to secondary flows and how much is an incidence effect on two-dimensional flow. Observing the huge growth of SKE (up to 3 percent of the outlet kinetic energy), it appears clear that important dissipations take place when the secondary vortices of the two half-channels interact each other.

This is supported also by the results at M_{2is} = 0.3 presented in Fig. 11. While at i = 0 the overall loss is only slightly higher than at M_{2is} = 0.7, at positive incidences the loss increase is substantially higher ($\bar{\zeta}$ grows up to 12 percent). Reducing the Mach number means the secondary flows shift toward the midspan (Perdichizzi, 1990), and therefore a strong interaction between counterrotating vortices, constrained in the midspan region, takes place.

The results plotted in Fig. 12 show that at design conditions Craig and Cox's correlation works reasonably well, as the level of the secondary losses is captured. But when the inlet angle is varied, both for positive and negative incidences, the relevant changes of the secondary losses are not adequately predicted, and large errors (up to 0.03) have been found.

Conclusions

The performance of a high-pressure steam turbine profile has been investigated for a wide range of off-design conditions. Detailed quantitative information has been reported for each combination of five incidence angles and three pitch-chord ratios. Data include profile Mach number distributions, area plots, spanwise deviation angle and loss distributions, profile and secondary losses.

The changes of the secondary flow structure in a downstream plane have been shown in detail. A clear relationship between the blade loading in the first part of the blade passage and the intensity of the secondary flows has been observed: High levels of streamwise vorticity and intense crossflows at the endwall take place at large incidence angles and low solidities. Heavy modifications have been found in the deviation angle distributions: The maximum overturning angle varies from almost zero up to 15 deg.

As the incidence angle and the pitch-chord ratio are increased, the region covered by secondary flows extends progressively toward the midspan. For extreme conditions the vortices of the two halves of the flow channel meet at midspan and interact with each other; as a consequence the overall secondary loss and the exit flow angle undergo a huge increase.

The application of the Craig and Cox's method provided

unrealistic secondary loss estimation, especially at inlet angles different from the design.

The comprehensive body of data here presented can be a useful reference for evaluating secondary flow effects in designing new turbines, or for establishing more up-to-date correlations for secondary loss and deviation angle prediction.

Finally, these data are also suitable to be utilized for assessing the accuracy of viscous three-dimensional methods, under quite different loading conditions, for which viscous effects vary significantly.

Acknowledgments

The authors wish to thank Ansaldo Componenti s.r.l. for the permission to publish the experimental data and Dr. M. Savini for the oil flow visualizations. The invaluable support by Mr. C. De Ponti and Mr. G. B. Daminelli is gratefully acknowledged.

References

Ainley, D. C., and Mathieson, G. C. R., 1951, "A Method of Performance Estimation for Axial-Flow Turbines," British Aeronautical Research Council, R&M 2974.

Bassi, F., and Perdichizzi, A., 1987, "Secondary Flow Development Downstream of a Turbine Cascade," *Proceedings 1987 Tokyo Gas Turbine Congress*, Vol. II, pp. 123–130.

Bassi, F., and Savini, M., 1992, "Secondary Flows in a Transonic Cascade: Validation of a Three-Dimensional Navier Stokes Code," ASME Paper No. 92-GT-62.

Craig, H. R., and Cox, H. J. A., 1971, "Performance Estimation of Axial Flow Turbines," *Proceedings of the Institution of Mechanical Engineers*, Vol. 185 32/71, pp. 403–423.

Dunham, J., and Came, P. M., 1970, "Improvement to the Ainley-Mathieson Method of Turbine Performance Prediction," ASME *Journal of Engineering for Power*, Vol. 92, pp. 252–256.

Gregory-Smith, D. G., Graves, C. P., and Walsh, J. A., 1988a, "Growth of Secondary Losses and Vorticity in an Axial Turbine Cascade," ASME JOURNAL OF TURBOMACHINERY, Vol. 110, pp. 1–8.

Gregory-Smith, D. G., Walsh, J. A., Graves, C. P., and Fulton, K. P., 1988b, "Turbulence Measurements and Secondary Flows in a Turbine Rotor Cascade," ASME JOURNAL OF TURBOMACHINERY, Vol. 110, pp. 479–485.

Hodson, H. P., and Dominy, R. G., 1987a, "Three-Dimensional Flow in a Low-Pressure Turbine Cascade at Its Design Condition," ASME JOURNAL OF TURBOMACHINERY, Vol. 109, pp. 177–185.

Hodson, H. P., and Dominy, R. G., 1987b, "The Off-Design Performance of a Low-Pressure Turbine Cascade," ASME JOURNAL OF TURBOMACHINERY, Vol. 109, pp. 201–209.

Langston, L. S., Nice, M. L., and Hooper, R. M., 1977, "Three-Dimensional Flow Within a Turbine Cascade Passage," ASME *Journal of Engineering for Power*, Vol. 1, pp. 21–28.

Marchal, P., and Sieverding, C. H., 1977, "Secondary Flows Within Turbomachinery Bladings," AGARD Conf. on Secondary Flow in Turbomachines, AGARD CP-214, Paper No. 11.

Moore, J., and Adhye, R. Y., 1985, "Secondary Flow and Losses Downstream of a Turbine Cascade," ASME *Journal of Engineering for Gas Turbines and Power*, Vol. 107, pp. 961–968.

Moore, J., Shaffer, D. M., and Moore, J. G., 1987, "Reynolds Stresses and Dissipation Mechanism Downstream of a Turbine Cascade," ASME JOURNAL OF TURBOMACHINERY, Vol. 109, pp. 258–267.

Osnaghi, C., and Perdichizzi, A., 1990, "Aerodynamic Measurements in Turbine Cascades at High Mach Number," *Proceedings of 10th Symposium on Measuring Techniques for Transonic and Supersonic Flows in Cascades and Turbomachines*, Von Karman Institute, Sept. 17–18.

Perdichizzi, A., Ubaldi, M., and Zunino, P., 1989, "Secondary Flows and Reynolds Stress Distributions Downstream of a Turbine Cascade at Different Expansion Ratios," AGARD Conf. on Secondary Flows in Turbomachines, AGARD CP-269, Paper No. 6.

Perdichizzi, A., 1990, "Mach Number Effects on Secondary Flow Development Downstream of a Turbine Cascade," ASME JOURNAL OF TURBOMACHINERY, Vol. 112, pp. 643–651.

Sharma, O. P., and Butler, T. L., 1987, "Predictions of Endwall Losses and Secondary Flows in Axial Flow Turbine Cascades," ASME JOURNAL OF TURBOMACHINERY, Vol. 109, pp. 229–236.

Sieverding, C. H., 1985, "Recent Progress in the Understanding of Basic Aspects of Secondary Flow in Turbine Blade Passages," ASME *Journal of Engineering for Gas Turbines and Power*, Vol. 107, pp. 248–257.

Yamamoto, A., 1987, "Production and Development of Secondary Flows and Losses in Two Types of Straight Turbine Cascades: Part 1: Stator Case," ASME JOURNAL OF TURBOMACHINERY, Vol. 108, pp. 186–193.

Yamamoto, A., and Nouse, H., 1988, "Effects of Incidence on Three-Dimensional Flows in a Linear Turbine Cascade," ASME JOURNAL OF TURBOMACHINERY, Vol. 110, pp. 486–496.

Zunino, P., Ubaldi, M., and Satta, A., 1987, "Measurements of Secondary Flows and Turbulence in a Turbine Cascade Passage," ASME Paper No. 87-GT-132.

APPENDIX

Blade Profile Coordinates

	X p.side	Y p.side		X s.side	Y s.side
1	0.0000	0.0000	56	33.9238	40.5980
2	0.1266	1.2015	57	33.6978	39.3938
3	0.5682	2.3260	58	33.4659	38.1907
4	1.2929	3.2927	59	33.2290	36.9807
5	2.2484	4.0319	60	32.9864	35.7878
6	3.3661	4.4902	61	32.7381	34.5880
7	4.5870	4.8152	62	32.4843	33.3895
8	5.7987	5.1725	63	32.2249	32.1920
9	6.9927	5.5851	64	31.9601	30.9958
10	8.1684	6.0474	65	31.6900	29.8008
11	9.3293	6.5455	66	31.4146	28.6069
12	10.4767	7.0742	67	31.1340	27.4143
13	11.6063	7.6398	68	30.8482	26.2229
14	12.7107	8.2531	69	30.5570	25.0329
15	13.7841	8.9192	70	30.2599	24.2367
16	14.8237	9.6369	71	29.9566	22.6572
17	15.8290	10.4020	72	29.6468	21.4719
18	16.7993	11.2108	73	29.3299	20.2884
19	17.7343	12.0603	74	29.0048	19.1071
20	18.6337	12.9475	75	28.6705	17.9284
21	19.4976	13.8693	76	28.3259	16.7527
22	20.3264	14.8226	77	27.9697	15.5805
23	21.1212	15.8047	78	27.6010	14.4121
24	21.8828	16.8126	79	27.2186	13.2481
25	22.6126	17.8438	80	26.8216	12.0890
26	23.3120	18.8959	81	26.4087	10.9355
27	23.9828	19.9665	82	25.9782	9.7885
28	24.6268	21.0534	83	25.5280	8.6490
29	25.8427	23.2681	84	25.0562	7.5184
30	26.4190	24.3924	85	24.5611	6.3978
31	26.9775	25.5256	86	24.0418	5.2881
32	27.5200	26.6666	87	23.4975	4.1904
33	28.0475	27.8146	88	22.9252	3.1072
34	28.5711	28.9689	89	22.3199	2.0421
35	29.0621	30.1287	90	21.6769	0.9993
36	29.5518	31.2932	91	20.9940	-0.0178
37	30.0317	32.4619	92	20.2691	-1.0054
38	30.5023	33.6344	93	19.4964	-1.9560
39	30.9640	34.8104	94	18.6701	-2.8603
40	31.4169	35.9898	95	17.7952	-3.7179
41	31.8524	37.1724	96	16.8745	-4.5259
42	32.2978	38.3580	97	15.8858	-5.2484
43	32.7259	39.5466	98	14.8302	-5.8695
44	33.1472	40.7379	99	13.7264	-6.4003
45	33.5603	41.9317	100	12.5720	-6.8085
46	33.6002	42.0093	101	11.3764	-7.0725
47	33.6608	42.0721	102	10.1571	-7.1834
48	33.7369	42.1149	103	8.9339	-7.1322
49	33.8221	42.1340	104	7.7277	-6.9220
50	33.9091	42.1278	105	6.5566	-6.5646
51	33.9908	42.0968	106	5.4319	-6.0800
52	34.0600	42.0437	107	4.3598	-5.4880
53	34.1111	41.9729	108	3.3440	-4.8037
54	34.1397	41.8905	109	2.3846	-4.0420
55	34.1444	41.8031	110	1.4855	-3.2103
			111	0.7048	-2.2883
			112	0.1975	-1.1919